J. Fluid Mech. (2001), *vol.* 436, *pp.* 207–230. Printed in the United Kingdom

Deformation of a two-dimensional viscous drop in time-periodic extensional flows: analytical treatment

By KAUSIK SARKAR AND WILLIAM R. SCHOWALTER

Department of Chemical Engineering, University of Illinois at Urbana-Champaign, Urbana, IL 61801, USA

(Received 20 October 1999 and in revised form 12 December 2000)

In Sarkar & Schowalter (2001), we reported results from numerical simulations of drop deformation in various classes of time-periodic straining flows at non-zero Reynolds number. As often occurs, analytical solutions provide more effective understanding of the structure and significance of a phenomenon. Here we describe drop deformation predicted from analytical solutions to linear time-periodic straining flows. Three different limiting cases are considered: an unsteady Stokes flow that retains all but the nonlinear advection terms, a Stokes flow that neglects inertia altogether, and an inviscid potential flow. The first limit is in clear contrast to the common approach in emulsion literature that resorts almost always to the Stokes flow assumption. The analysis clearly shows the forced–damped mass–spring system underlying the physical phenomena, which distinguishes it from the inertialess Stokes flow. The potential flow also depicts resonance, albeit of an undamped system, and provides an important limit of the problem. The drop deformation is assumed to be small, and a perturbative approach has been employed. The first-order problem has been solved to arrive at either an evolution equation (in Stokes and potential flow limits) or the long-time periodic drop response (for unsteady Stokes analysis). The analytical results compare satisfactorily with those obtained from the numerical simulation in Sarkar & Schowalter (2001), and the resonance characteristics are quantitatively explained. The three different solutions are compared with each other, and the results are presented for different parameters such as frequency, interfacial tension, viscosity ratio, density ratio and Reynolds number. Furthermore, the simple ODE model presented in the Appendix of Sarkar & Schowalter (2001) is shown to explain the asymptotic limits of the present solution.

1. Introduction

Drop deformation and breakup have been objects of continuing study through most of this century. Taylor (1932) employed Lamb's general solution (1887, 1932 p. 596) for Stokes flow in spherical coordinates to find equilibrium drop shapes, and validated them by comparison to experiments with a four-roll mill apparatus. Also relevant to the present work is the study by Cox (1969), who for the first time performed a systematic perturbation analysis for small drop deformation. He arrived at a time evolution equation for drop shape using again Lamb's solution. Cox's result has been improved to higher orders by Frankel & Acrivos (1970), and Barthès-Biesel & Acrivos (1973). Following work on the effect of vorticity by Hakimi & Schowalter (1980), Rallison (1980, 1984) put the evolution equation into

a unified general framework. Since then the general equation (Rallison 1980) has been compared with experimental observations (Bentley & Leal 1986*a*, *b*). The effect of linear flows with different symmetric and anti-symmetric parts has been studied and collated (for a recent review see Stone 1994). The forcing flows are generated by four-roll mills.

The present work arose from a proposal to use a different experimental flow for deformation studies, namely a potential vortex. The potential vortex provides effects of time dependence, a crucial component for complex rheological flows, and has important implications for turbulent flows of emulsions and polymeric fluids. To establish the viability of this flow as a valuable study tool, it has been numerically simulated (Sarkar & Schowalter 2001, henceforth referred to as SS1). In our numerical efforts we were led to other classes of linear time-dependent flows that are of interest in drop deformation. Unlike past simulations that largely concentrated on the Stokes limit (except for Seth & Pozrikidis 1995), ours has been a simulation at finite Reynolds number. Owing to the finite inertia, a number of new and interesting phenomena occur (see SS1 for details), such as non-monotonicity of deformation with time and reversal of axes of stretching and squeezing even in a steady flow, and a resonance phenomenon for time-periodic flows. In a time-periodic flow the drop deformation amplitude is seen to increase to a peak with increasing interfacial tension before finally decreasing. One would expect the interfacial tension to inhibit deformation. The phenomenon has been attributed to a harmonic oscillator underlying the flow, and a simple model has been offered in the Appendix of SS1 to describe it. It is argued that the finite Reynolds number of the simulation furnishes a 'mass' term to the system, with interfacial tension and viscosity playing the role of spring constant and damping, respectively. Therefore changing interfacial tension leads to varying natural frequency, and maximum response occurs when it matches the forcing frequency.

In this article we undertake an analytical approach. Our aim is to provide a better understanding of the underlying mechanics. We treat the drop deformation in a perturbative way, as was done by previous researchers such as Cox (1969), Frankel & Acrivos (1970) and Rallison (1980). We focus on non-vortical extensional forcing flows as in SS1. However, even in a vortical flow essentially the same phenomena would be observed with different quantitative details. All previous analytical efforts with Stokes flows were performed in three dimensions, barring Richardson (1968, 1973) for viscosity ratio $\lambda = 0$, and Buckmaster & Flaherty (1973) for $\lambda = 1$. In conformity with the numerical work in SS1, we perform this analysis in two dimensions, and for time-dependent flows and drop shapes. Furthermore, our efforts differ significantly from others, in that we solve the unsteady Stokes problem retaining the linear inertia term, which, we will see, is essential to capture resonance. For reference we also perform an inertialess Stokes analysis for the two-dimensional time-dependent case. An inviscid analysis of the deformation is also furnished as an important mathematical limit. One should note that the unsteady Stokes problem has been solved in the frequency domain, recovering only the long-time periodic response, whereas the Stokes and the potential flows have been solved in the time domain to arrive at an evolution equation for the deformation. The present analytical work is also compared with the simple ODE model provided in the Appendix of SS1.

In § 2, we provide a mathematical formulation of the problem with relevant non-dimensionalization and the appropriate conditions for arriving at the governing equations. In § 3, we introduce the perturbative expression. In § 4, we solve the zeroth-order problem in detail. Section 5 briefly describes the Stokes solution of the same problem. Inviscid analysis is taken up in § 6. Section 7 sets the stage for

comparison with numerical simulation by describing the different classes of time-periodic extensional flows. The results are described in § 8 and summarized in § 9.

2. Mathematical formulation

2.1. *Governing equations*

The velocity field $\boldsymbol{u}$ and the pressure p satisfy the equation of momentum conservation

$$\frac{\partial(\rho u_i)}{\partial t} + \partial_j(\rho u_i u_j) = -\partial_i p + \mu\nabla^2 u_i, \tag{2.1}$$

in the continuous phase domain Ω_c. In the suspended drop Ω_d the corresponding equation is

$$\frac{\partial(\rho^* u_i^*)}{\partial t} + \partial_j(\rho^* u_i^* u_j^*) = -\partial_i p^* + \mu^*\nabla^2 u_i^*, \tag{2.2}$$

where ρ is the density, and μ viscosity. Quantities inside the drop are represented by an asterisk. Mass conservation results in

$$\partial_i u_i = \partial_i u_i^* = 0. \tag{2.3}$$

The boundary conditions at the drop interface ∂B are given by the velocity and stress continuity

$$u_i n_i = u_i^* n_i, \tag{2.4}$$

$$u_i - u_j n_j n_i = u_i^* - u_j^* n_j n_i, \tag{2.5}$$

$$n_i(p_{ij} - p_{ij}^*)n_j = \sigma\mathscr{C}, \tag{2.6}$$

$$p_{ij}n_j - (n_k p_{kj} n_j)n_i = p_{ij}^* n_j - (n_k p_{kj}^* n_j)n_i, \tag{2.7}$$

where $\mathscr{C}$ is the interface curvature, and σ interfacial tension. The stress tensor p_{ij} follows from the Newtonian constitutive law

$$p_{ij} = -p\delta_{ij} + 2\mu e_{ij}, \quad e_{ij} = \tfrac{1}{2}(\partial_i u_j + \partial_j u_i). \tag{2.8}$$

The surface evolution is governed by the kinematic condition

$$\frac{\mathrm{D}\mathscr{F}}{\mathrm{D}t} \equiv \frac{\partial\mathscr{F}}{\partial t} + u_i\partial_i\mathscr{F} = \frac{\partial\mathscr{F}}{\partial t} + K n_i u_i = 0, \tag{2.9}$$

where $\mathscr{F}(\boldsymbol{x};t) = 0$ is the equation of the drop interface, $K^{-1} = |\nabla\mathscr{F}|$.

We non-dimensionalize the above equations with time scale $\dot\gamma^{-1}$, length scale a, velocity scale $\dot\gamma a$, and pressure and stresses by $\mu\dot\gamma$. Inside the drop the corresponding material properties are used. Furthermore, the following time dependence is assumed for all dependent variables:

$$\boldsymbol{u} = \boldsymbol{u}'\mathrm{e}^{\mathrm{i}\omega t}, \quad p = p'\mathrm{e}^{\mathrm{i}\omega t}, \ldots . \tag{2.10}$$

Dropping the prime, and retaining the same notation for the non-dimensionalized variables, we arrive at the final forms

$$-\alpha^2 u_i = -\partial_i p + \nabla^2 u_i + O(Re), \tag{2.11}$$

$$-\alpha^{*2} u_i^* = -\partial_i p^* + \nabla^2 u_i^* + O(Re^*), \tag{2.12}$$

where $\alpha^2 = -\mathrm{i}St\,Re$, $\alpha^{*2} = -\mathrm{i}St\,Re^*$, $Re = (\rho\dot\gamma a^2)/\mu$ is the Reynolds number, $Re^* = \lambda_\rho Re/\lambda$, $\lambda = \mu^*/\mu$, and $\lambda_\rho = \rho^*/\rho$. $St = \omega/\dot\gamma$ is the Strouhal number. (We choose

positive real part for $\sqrt{-\mathrm{i}}$, i.e. $\alpha = (1-\mathrm{i})\sqrt{St\,Re/2}$, that leads to the Bessel function of the second kind $H_n^{(2)}$ later). We have dropped the nonlinear inertial term that is of $O(Re)$, but have kept the unsteady term that is $O(St\,Re)$. Combining normal velocity conditions (2.4) with the kinematic interfacial condition (2.9), and writing explicitly the surface representation as

$$\mathscr{F} \equiv r - 1 - \mathscr{G}, \tag{2.13}$$

with periodic $\mathscr{G}$, we obtain

$$K u_i n_i = K u_i^* n_i = iSt\mathscr{G} \equiv \beta\mathscr{G}. \tag{2.14}$$

The relations (2.3) and (2.5) remain unchanged in form. The normal stress condition (2.6) becomes

$$n_i(p_{ij} - \lambda p_{ij}^*)n_j = k\mathscr{C}, \tag{2.15}$$

$k = \sigma/(\dot{\gamma}\mu a)$ being the inverse of the capillary number. The tangential stress continuity (2.7) becomes

$$p_{ij}n_j - (n_k p_{kj} n_j)n_i = \lambda\{p_{ij}^* n_j - (n_k p_{kj}^* n_j)n_i\}. \tag{2.16}$$

The above procedure has established the governing equations and the concomitant boundary conditions for the problem. In earlier studies researchers resorted to steady Stokes flow, assuming the Reynolds number of the problem to be sufficiently small to validate such an approximation. However for high-frequency oscillation, St could be sufficiently large to require retention of the linear unsteady term (Landau & Lifschitz 1987, p. 83; Lamb 1932, p. 632). We shall see that the linear acceleration term is essential to match the behaviour observed in our numerical simulation at small but non-zero Reynolds number.

3. Perturbative solution

In the literature for drop deformation at zero Reynolds number, it was recognized that the drop evolution problem can be solved as a perturbation on the initial circular (spherical in three dimensions) surface. It also became evident that there are two small parameters controlling the extent of the deformation, namely $1/\lambda$ and $1/k$–representing, respectively, flows that are dominated by high viscosity ratio and large interfacial tension. In our case drop deformation could also be small because of large St, i.e. high-frequency oscillatory $\boldsymbol{u}^\infty$. We solve for linear stretching forcing flow, i.e.

$$u_i^\infty = E_{ij}x_j, \qquad u_i \to u_i^\infty, \quad x_i \to \infty, \tag{3.1}$$

with E_{ij} traceless (incompressibility) and symmetric (extensional). This undisturbed flow field satisfies the governing equation (2.11), with

$$p^\infty = \tfrac{1}{2}\alpha^2 x_i E_{ij} x_j. \tag{3.2}$$

We can formally expand all dependent variables in powers of a small parameter ϵ following Cox (1969):

$$u_i - u_i^\infty = u_i^{(0)} + \epsilon u_i^{(1)} + \epsilon^2 u_i^{(2)} + \cdots, \tag{3.3}$$

$$p = p^{(0)} + \epsilon p^{(1)} + \epsilon^2 p^{(2)} + \cdots, \tag{3.4}$$

and their starred counterparts inside the drop. The drop interface function is expressed as

$$\mathscr{G} = \epsilon f = f^{(0)} + \epsilon f^{(1)} + \epsilon^2 f^{(2)} + \cdots. \tag{3.5}$$

Using these expressions, it is easily seen that the same governing equations (2.11) and (2.12) are satisfied by the zeroth-order variables. We restrict ourselves to flows dominated by large interfacial tension rather than those where the viscosity ratio is high. Hence we assume $k = O(\epsilon^{-1})$, $\lambda = O(1)$. As was shown by Cox (1969), and Frankel & Acrivos (1970), one can solve the high-λ limit. However, in the present unsteady case, owing to the additional complexity of the eigenfunctions, the procedure is not entirely trivial, even though it is conceptually analogous.

At the boundaries, the zeroth-order variables satisfy the tangential velocity and stress continuity conditions (2.5) and (2.16). The treatment for the normal velocity (2.14) involves some subtlety. From (3.5), we note that the right-hand side of (2.14) is $O(\epsilon)$. Therefore formally in the zeroth order, the drop (2.13) remains an undeformed circle, and hence the normal velocity at the inside and the outside surface individually vanishes. One would not need a normal stress condition at this order. However the zeroth-order solution (with circular drop) does not provide any deformation information, necessitating a further first-order analysis. For the three-dimensional Stokes analysis Cox (1969) followed this approach to obtain the surface evolution equation at the first order, with the first-order problem solved only partially. This fact was noted by Frankel & Acrivos (1970), who showed that the same evolution equation for the surface function $f(\theta)$ could be obtained in a single step by retaining the $\epsilon\,\partial f^{(0)}/\partial t$ (in our case $\mathrm{i}\epsilon St f^{(0)}$) in the zeroth order. In this case, to zeroth order, the normal velocities at the surface are not zero, but equal to the first-order surface evolution term. In this way the all-important surface evolution term, even though formally of smaller order $O(\epsilon)$, is brought to act in the zeroth order. One can also provide a formal justification of this procedure by claiming that the time-derivative term itself is sufficiently large ($\beta = O(1/\epsilon)$ at least) (see (2.14)). Hence it makes its appearance in the zeroth order. In other words, as Frankel & Acrivos (1970) claim, even though $\epsilon f^{(0)}$ is $O(\epsilon)$, $\epsilon\partial f^{(0)}/\partial t$ need not be. However as long as the ϵ of this time-derivative term is carried through in this zeroth-order analysis, one arrives at the result, obtained in the conventional way of Cox (1969). We follow here the shorter single-step approach of Frankel & Acrivos (1970). The equation (2.14), becomes at $r = 1$

$$u_i^{(0)} n_i = u_i^{*(0)} n_i = \epsilon\beta f^{(0)} + O(\epsilon). \tag{3.6}$$

Noting that the curvature is given by

$$\mathscr{C} = \nabla \cdot \boldsymbol{n} = \nabla \cdot \frac{\nabla \mathscr{F}}{|\nabla \mathscr{F}|} = \frac{1}{r} - \frac{1}{r^2}\epsilon f''(\theta) + O(\epsilon^2), \tag{3.7}$$

the normal stress condition (2.15) with $k = \epsilon^{-1}$, at zeroth order becomes for $r = 1$,

$$n_i(p_{ij}^{(0)} - \lambda p_{ij}^{*(0)})n_j = n_i k(1 - \epsilon f^{(0)''}) + O(\epsilon). \tag{3.8}$$

The first term on the right-hand side, appearing from the surface curvature of the undisturbed circular shape, is evidently $O(\epsilon^{-1})$. However its presence in the zeroth order is an artifact of the shorter one-step method that we have undertaken. Cox (1969) did not assume *a priori* any order for λ or k. In his work the inside pressure (T_0^*) remains indeterminate in the zeroth-order analysis, only to be balanced by surface curvature in the first order. Here also it would be seen that this term would account for the constant term in the internal pressure p^*. A formal approach would

be to keep an ϵ^{-1} term in the expressions for pressures, its existence justified in view of the first term in the right-hand side of (3.8). Then at that lowest order they would have balanced each other.

4. Zeroth order

We drop the superscript (0) for convenience, keeping in mind that all the variables below are of zero order. The velocity may conveniently be represented by a Helmholtz decomposition

$$\boldsymbol{u} = \boldsymbol{u}^{\infty} + \nabla\phi + \nabla \times \psi\hat{\boldsymbol{k}}, \tag{4.1}$$

$$\boldsymbol{u}^{*} = \nabla\phi^{*} + \nabla \times \psi^{*}\hat{\boldsymbol{k}}, \tag{4.2}$$

and we arrive at the following set of governing equations:

$$\nabla^2 p = \nabla^2 p^{*} = \nabla^2\phi = \nabla^2\phi^{*} = 0, \tag{4.3}$$

$$\phi = \frac{1}{\alpha^2}(p - p^{\infty}), \quad \phi^{*} = \frac{1}{\alpha^{*2}}p^{*}, \tag{4.4}$$

and

$$(\nabla^2 + \alpha^2)\psi = (\nabla^2 + \alpha^{*2})\psi^{*} = 0. \tag{4.5}$$

We can write down the general solution for the above set of equations:

$$p - p^{\infty} = \alpha^2\phi = \sum_n \left(T_n \cos n\theta + \tilde{T}_n \sin n\theta\right) r^{-n}, \tag{4.6}$$

$$p^{*} = \alpha^{*2}\phi^{*} = \sum_n \left(T_n^{*} \cos n\theta + \tilde{T}_n^{*} \sin n\theta\right) r^{n}, \tag{4.7}$$

$$\psi = \sum_n \left(U_n \cos n\theta + \tilde{U}_n \sin n\theta\right) H_n^{(2)}(\alpha r), \tag{4.8}$$

$$\psi^{*} = \sum_n \left(U_n^{*} \cos n\theta + \tilde{U}_n^{*} \sin n\theta\right) J_n(\alpha^{*} r), \tag{4.9}$$

where $H_n^{(2)} = J_n - \mathrm{i}Y_n$ is the Bessel function of the third kind, and J_n and Y_n are ordinary Bessel functions. The regularity at $r = 0$ and $r \to \infty$ have been taken into account (recall α has been chosen to have positive real part), to obtain the proper Bessel function outside the drop ($H_n^{(2)}(z) \sim \sqrt{2/(\pi z)} \exp -\mathrm{i}(z - 0.5nz - 0.25\pi)$). T_n, U_n and their starred and tilded counterparts are coefficients defining the analytic expressions. The surface deformation function is expanded as

$$f(\theta) = \sum_n (f_n \cos n\theta + \tilde{f}_n \sin n\theta). \tag{4.10}$$

Applying the boundary conditions (3.6), (3.8), and (2.16), we obtain for the zeroth-order variables

$$u_r = \epsilon\beta f, \tag{4.11}$$

$$u_r^{*} = \epsilon\beta f, \tag{4.12}$$

$$u_\theta - u_\theta^{*} = 0 \tag{4.13}$$

$$p_{rr} - \lambda p_{rr}^{*} = k(1 - \epsilon f'') \tag{4.14}$$

$$p_{r\theta} - \lambda p_{r\theta}^{*} = 0. \tag{4.15}$$

Detailed expressions for velocities and stresses evaluated at $r = 1$ are provided in Appendix A.

It has been recognized by Cox (1969) that for an initially circular drop, only the second harmonics survive, owing to the linear forcing field assumed at infinity. There is, however, the constant term k due to curvature in (4.14). As mentioned before, it is balanced by the pressure jump. We note that $p \to p^{\infty}$, as $\boldsymbol{x} \to \infty$. Hence for $n = 0$ all the coefficients are zero except for

$$\lambda T_0^* = k. \tag{4.16}$$

Henceforth we concentrate on $n = 2$. The boundary conditions on the normal (two: inside and outside) and tangential velocities, and the tangential stress afford provide equations for four unknowns T_2, T_2^*, U_2, U_2^*, and similarly for the corresponding coefficients (with tildes) for the $\sin 2\theta$ terms. For the normal velocity conditions we obtain the following equations:

$$-\frac{2}{\alpha^2} T_2 + 2H_2 \tilde{U}_2 = \epsilon\beta f_2 - E_{11}, \tag{4.17}$$

$$-\frac{2}{\alpha^2} \tilde{T}_2 - 2H_2 U_2 = \epsilon\beta \tilde{f}_2 - E_{12}, \tag{4.18}$$

$$\frac{2}{\alpha^{*2}} T_2^* + 2J_2 \tilde{U}_2^* = \epsilon\beta f_2, \tag{4.19}$$

$$\frac{2}{\alpha^{*2}} \tilde{T}_2^* - 2J_2 U_2^* = \epsilon\beta \tilde{f}_2. \tag{4.20}$$

For the tangential velocity conditions, we obtain

$$\frac{2}{\alpha^2} \tilde{T}_2 - \frac{2}{\alpha^{*2}} \tilde{T}_2^* - \alpha H_2' U_2 + \alpha^* J_2' U_2^* = -E_{12}, \tag{4.21}$$

$$-\frac{2}{\alpha^2} T_2 + \frac{2}{\alpha^{*2}} T_2^* - \alpha H_2' \tilde{U}_2 + \alpha^* J_2' \tilde{U}_2^* = E_{11}. \tag{4.22}$$

The tangential traction continuity affords

$$-\frac{6}{\alpha^2} \tilde{T}_2 - \frac{2\lambda}{\alpha^{*2}} \tilde{T}_2^* - \alpha^2 \left(H_2'' + \tfrac{1}{2} H_2\right) U_2 + \lambda\alpha^{*2} \left(J_2'' + \tfrac{1}{2} J_2\right) U_2^* = -E_{12}, \tag{4.23}$$

$$\frac{6}{\alpha^2} T_2 + \frac{2\lambda}{\alpha^{*2}} T_2^* - \alpha^2 \left(H_2'' + \tfrac{1}{2} H_2\right) \tilde{U}_2 + \lambda\alpha^{*2} \left(J_2'' + \tfrac{1}{2} J_2\right) \tilde{U}_2^* = E_{11}, \tag{4.24}$$

and the normal traction,

$$-\left(1 - \frac{12}{\alpha^2}\right) T_2 + \left(1 - \frac{4}{\alpha^2}\right) \lambda T_2^* - 4(H_2 - \alpha H_2') \tilde{U}_2 + 4(J_2 - \alpha^* J_2') \lambda \tilde{U}_2^* = \left(\frac{\alpha^2}{2} - 2\right) E_{11} + 4k\epsilon f_2, \tag{4.25}$$

$$-\left(1 - \frac{12}{\alpha^2}\right) \tilde{T}_2 + \left(1 - \frac{4}{\alpha^2}\right) \lambda \tilde{T}_2^* + 4(H_2 - \alpha H_2') U_2 - 4(J_2 - \alpha^* J_2') \lambda U_2^* = \left(\frac{\alpha^2}{2} - 2\right) E_{12} + 4k\epsilon \tilde{f}_2. \tag{4.26}$$

The set of equations has been solved in Appendix B, and the periodic drop shape

relating to imposed strain rate (B 9) has been obtained:

$$\{\beta(D_1C_2 + D_2C_4 - D_3B_2 - D_4B_4) - 4k\} \begin{pmatrix} \epsilon f_2 \\ \epsilon \tilde{f}_2 \end{pmatrix} = \left(\frac{\alpha^2}{2} - 2 - D_1C_1 - D_2C_3 + D_3B_1 + D_4B_3\right) \begin{pmatrix} E_{11} \\ E_{12} \end{pmatrix}. \quad (4.27)$$

Equation (4.27), with the coefficients defined in Appendix B, is the final result of our analysis of the unsteady Stokes problem for finding the drop shape in a time-periodic extensional flow. Note that because of the assumed time-periodicity of the solution, it provides only the amplitude.

5. Stokes limit

For completeness we include a Stokes solution of a two-dimensional drop deformation. The approach is similar to that of Cox (1969) or Frankel & Acrivos (1970). Hence details are omitted. In the Stokes limit the governing equations (2.11) and (2.12) reduce to

$$-\partial_i p + \nabla^2 u_i = 0, \quad (5.1)$$

$$-\partial_i p^* + \nabla^2 u_i^* = 0, \quad (5.2)$$

with the usual zero divergence condition for the velocity fields. Assuming

$$\boldsymbol{u} = \nabla \times \psi \hat{k}, \qquad \boldsymbol{u}^* = \nabla \times \psi^* \hat{k}, \quad (5.3)$$

we obtain

$$\nabla^4 \psi = \nabla^4 \psi^* = 0. \quad (5.4)$$

The stress and the tangential velocity boundary conditions remain the same as (2.15), (2.16) and (2.5) in their non-dimensional forms. However for the normal velocity/kinematic condition the following consideration appears. In the unsteady Stokes solution we are forced into making an assumption of periodic variation in time (2.10). In other words, a Fourier transform in time was performed on the boundary-value problem. In contrast here, because the governing equations do not involve a time derivative, we need not assume *a priori* periodic variation. Therefore, instead of (2.14), the original condition (2.9) becomes

$$K u_i n_i = K u_i^* n_i = -\frac{\partial \mathscr{F}}{\partial t}, \quad (5.5)$$

and one arrives at a time evolution equation. In contrast, for the unsteady Stokes analysis we obtain the Fourier transform (4.27) of the evolution function, which is only a measure of its long-term steady periodic response. In other words, for the unsteady Stokes analysis the problem is solved in the frequency domain, while here it is solved in the time domain. However, for comparison we will later resort to the periodic assumption.

One can execute a perturbative analysis following the treatment in § 3, to obtain the same governing equations (5.4) in all orders, and more specifically in zeroth order which is of interest here. The general solution of the biharmonic equation is provided by Fung (1965, p. 246). Following the discussion for the unsteady Stokes problem, we restrict the solution to the second harmonic ($n = 2$), with the caveat that the constant part ($n = 0$) of the internal pressure supports the interfacial force arising from the

undisturbed curvature of the drop. The solution is given by

$$\psi = (U_2 r^{-2} + \tilde{T}_2)\cos 2\theta + (\tilde{U}_2 r^{-2} + T_2)\sin 2\theta, \tag{5.6}$$

$$\psi^* = (U_2^* r^2 + \tilde{T}_2^* r^4)\cos 2\theta + (\tilde{U}_2^* r^2 + T_2^* r^4)\sin 2\theta. \tag{5.7}$$

One can find the pressure by integrating (5.1) and (5.2)

$$p = 4(T_2 \cos 2\theta - \tilde{T}_2 \sin 2\theta) r^{-2}, \tag{5.8}$$

$$p^* = 12(T_2^* \cos 2\theta - \tilde{T}_2^* \sin 2\theta) r^2. \tag{5.9}$$

Expressions for stresses and velocities are provided in Appendix C. The interface conditions provide the following set of equations for the normal velocity:

$$-2(U_2 + \tilde{T}_2) = \epsilon \frac{\partial \tilde{f}_2}{\partial t} - E_{12}, \tag{5.10}$$

$$2(\tilde{U}_2 + T_2) = \epsilon \frac{\partial f_2}{\partial t} - E_{11}, \tag{5.11}$$

$$-2(U_2^* + \tilde{T}_2^*) = \epsilon \frac{\partial \tilde{f}_2}{\partial t}, \tag{5.12}$$

$$2(\tilde{U}_2^* + T_2^*) = \epsilon \frac{\partial f_2}{\partial t}. \tag{5.13}$$

For the tangential velocity, we obtain

$$2U_2 + 2U_2^* + 4\tilde{T}_2^* = -E_{12}, \tag{5.14}$$

$$2\tilde{U}_2 + 2\tilde{U}_2^* + 4T_2^* = E_{11}. \tag{5.15}$$

The tangential traction continuity requires

$$-(6U_2 + 2\tilde{T}_2) + \lambda(2U_2^* + 6\tilde{T}_2^*) = -E_{12}, \tag{5.16}$$

$$-(6\tilde{U}_2 + 2T_2) + \lambda(2\tilde{U}_2^* + 6T_2^*) = E_{11}. \tag{5.17}$$

Finally, normal stress continuity gives rise to

$$12U_2 + 8\tilde{T}_2 + 4\lambda U_2^* = -2E_{12} + 4k\epsilon\tilde{f}_2, \tag{5.18}$$

$$-12\tilde{U}_2 - 8T_2 - 4\lambda\tilde{U}_2^* = -2E_{11} + 4k\epsilon f_2. \tag{5.19}$$

Like the case of the unsteady Stokes flow, the set of equations can similarly be solved to arrive at the equation of surface evolution

$$3(1+\lambda)\frac{\partial \epsilon f_2}{\partial t} + 4k\epsilon f_2 = 6E_{11}, \tag{5.20}$$

and an identical equation relating $\tilde{f}_2$ and E_{12}. This equation is the two-dimensional analogue of the equation given by Frankel & Acrivos (1970) in the first order. They then went on to furnish the second-order solution. Here our aim is to provide a comparison with the unsteady Stokes flow, and the numerical results obtained in SS1. The first-order solution will suffice for that purpose. Note that for $\lambda = 1, k = 0$ we obtain, as expected, a drop passively following the imposed flow. Assuming periodicity, we make the substitution $\partial/\partial t \rightarrow \mathrm{i}St = \beta$, and obtain the relation for the amplitude

$$[3(1+\lambda)\beta + 4k]\begin{pmatrix} \epsilon f_2 \\ \epsilon \tilde{f}_2 \end{pmatrix} = 6\begin{pmatrix} E_{11} \\ E_{12} \end{pmatrix}, \tag{5.21}$$

which is to be compared with (4.27). Note the similarity of the expression with (A6) from the model oscillator in Appendix of SS1, with $\widehat{Re} = 0$ and $\beta = \mathrm{i}\widehat{St}$ in the latter.

In this Stokes limit, one can solve the initial value problem (5.20) with initial condition $f_2(t = 0) = 0$, as

$$\epsilon f_2(t) = \frac{6E_{11}\mathrm{e}^{\beta t}}{3(1+\lambda)\beta + 4k}(1 - \mathrm{e}^{-(\delta+\beta)t}), \qquad \delta = \frac{4k}{3(1+\lambda)}, \tag{5.22}$$

with an analogous equation for $\tilde{f}_2$ (see (A5) in SS1). With $t \to \infty$, we recover (5.21). Note that in our unsteady Stokes analysis explicit time dependence in the differential equations precluded a time-domain analysis, and therefore we could only furnish the long-time periodic response. One could in principle solve an initial value problem for the unsteady Stokes case with numerical inversion of the Fourier transform (4.27). However, in our present two-dimensional case the effort seems to be unjustified, and the long-time periodic response seems to be adequate in describing the underlying physics.

6. Inviscid limit

We are primarily interested in the oscillatory behaviour of the drop. In conformity with this goal here we perform a purely inviscid analysis of the problem. The problem, being simpler and hence amenable to complete unsteady analysis, is of independent interest, and we provide a brief description of the procedure. The governing equations and boundary conditions of the problem in dimensional variables (we cannot perform the same non-dimensionalization as before for viscosities are zero here) are

$$\boldsymbol{u} = \nabla\phi, \qquad \boldsymbol{u}^* = \nabla\phi^*, \tag{6.1}$$

where ϕ and ϕ^* are potential functions. Linearized Bernoulli's equations relate the potential and the pressure

$$\rho\frac{\partial\phi}{\partial t} = -p, \qquad \rho^*\frac{\partial\phi^*}{\partial t} = -p^*. \tag{6.2}$$

The appropriate boundary conditions at the drop interface ($r = a$ in the perturbation analysis) are the pressure balance

$$-p - p^\infty + p^* = \sigma\mathscr{C} = \frac{\sigma}{a}\left(1 - \frac{1}{a}\epsilon f''\right) + O(\epsilon^2), \tag{6.3}$$

and the kinematic condition

$$\frac{\partial\phi}{\partial r} + u_r^\infty = \frac{\partial\phi^*}{\partial r} = \epsilon\frac{\partial f}{\partial t} + O(\epsilon^2). \tag{6.4}$$

The equations are then non-dimensionalized by scaling the length and time with a and $\dot{\gamma}^{-1}$, respectively, as before, but the pressure with $\rho\dot{\gamma}^2a^2$ We perform a series expansion in ϵ, and note that

$$p^\infty = \tfrac{1}{2}E_{ij}x_ix_j. \tag{6.5}$$

Similar to (4.6), and (4.7), we express the potentials at zeroth order as

$$\phi = \sum_n \left(T_n\cos n\theta + \tilde{T}_n\sin n\theta\right)r^{-n}, \qquad \phi^* = \sum_n \left(T_n^*\cos n\theta + \tilde{T}_n^*\sin n\theta\right)r^n. \tag{6.6}$$

After some analysis, one arrives at the following equation for the surface function (for the second harmonic $n = 2$):

$$\left[\tfrac{1}{2}(1+\lambda_\rho)\frac{\partial^2}{\partial^2 t} + 4k'\right]\epsilon f_2 = \dot{E_{11}}, \tag{6.7}$$

and an identical equation for $\tilde{f}_2$ relating to $\dot{E_{12}}$. Here $k' = \sigma/(\rho\dot{\gamma}^2 a^3)$. Making the substitution $\partial/\partial t \to \mathrm{i}St = \beta$, we obtain

$$\left[\tfrac{1}{2}(1+\lambda_\rho)\beta^2 + 4k'\right]\begin{pmatrix} \epsilon f_2 \\ \epsilon \tilde{f}_2 \end{pmatrix} = \beta \begin{pmatrix} E_{11} \\ E_{12} \end{pmatrix}. \tag{6.8}$$

In fact this equation could also be obtained by taking the limit $\alpha^2 \to \infty, k \to \infty, k' = k/Re, B_{1,2,3,4} = 0$ of the viscous equation (4.27). Note that resonance occurs at the frequency, $St = 2\sqrt{2k'/(1+\lambda_\rho)}$. Also note that similar equations (A7) and (A8) for the potential limit are provided in the Appendix of SS1.

7. Different time-periodic flows

We have numerically simulated a number of time-periodic flows in SS1. For quantitative comparison of those numerical results with their analytical counterparts in this article, one must relate the forcing fields and results properly. The rotating extensional (RE) flow could be written in dimensional variables as

$$\boldsymbol{u}_0^{\mathrm{RE}}(\boldsymbol{x}) = \boldsymbol{E}(t)\cdot\boldsymbol{x} = \dot{\gamma}\begin{pmatrix} \sin\omega t & -\cos\omega t \\ -\cos\omega t & -\sin\omega t \end{pmatrix}\cdot\begin{pmatrix} x \\ y \end{pmatrix}, \tag{7.1}$$

which, under the restriction $\omega = 2\dot{\gamma}$, becomes the linear approximant to a potential vortex flow $\boldsymbol{u}_0^{\mathrm{V}}$. The flow is extensional in nature. However, the axis of extension is rotating in the plane of the flow. Now in view of the periodic assumption (2.10) that has been invoked for the unsteady Stokes solution, the strain rate tensor is decomposed as follows:

$$\boldsymbol{E}(t) = E_{11}(t)\begin{pmatrix} 1 & 0 \\ 0 & -1 \end{pmatrix} + E_{12}(t)\begin{pmatrix} 0 & 1 \\ 1 & 0 \end{pmatrix}, \tag{7.2}$$

where

$$E_{11}(t) = \dot{\gamma}\sin\omega t, \qquad E_{12}(t) = -\dot{\gamma}\cos\omega t. \tag{7.3}$$

We have successfully reduced the forcing flow into time-periodic components, and hence we can use the solution (4.27). The relation (7.3) leads to $\tilde{f}_2 = -f_2$. Therefore we obtain in the zeroth order in ϵ

$$f(t) = \mathrm{Im}[f_2 \mathrm{e}^{\mathrm{i}\omega t}]\cos 2\theta - \mathrm{Re}[f_2 \mathrm{e}^{\mathrm{i}\omega t}]\sin 2\theta. \tag{7.4}$$

By writing $f_2 = A(\cos\Lambda + \mathrm{i}\sin\Lambda)$ for some A and Λ, we obtain for the surface

$$r - a = \epsilon f = \epsilon A \sin(\Lambda + \omega t - 2\theta). \tag{7.5}$$

It is seen that in this order the surface is an ellipse, and the long-time solution does not change shape, but rotates as has indeed been observed in SS1. The deformation $D = (L-l)/(L+l)$ (L is the maximum distance of the drop surface from the centre of the drop, and l the minimum distance) could be calculated to be

$$aD = \epsilon|f_2| = \epsilon A. \tag{7.6}$$

An oscillatory extensional (OE) flow (used in SS1) is given by

$$\boldsymbol{u}_0^{\mathrm{OE}} = -\dot{\gamma}\cos\omega t \begin{pmatrix} 0 & 1 \\ 1 & 0 \end{pmatrix} \cdot \begin{pmatrix} x \\ y \end{pmatrix}. \tag{7.7}$$

The extensional flow here is stretching and squeezing alternately along two fixed orthogonal directions. Correspondingly the surface $f(t)$ would involve only the second term of the relation (7.4), and then we obtain

$$r - a = \epsilon f = -\epsilon A \cos(\Lambda + \omega t)\sin 2\theta. \tag{7.8}$$

Here, in contrast to the rotating extensional flow, the shape changes, continually expanding and contracting in orthogonal directions, passing through a circle ($D = 0$). The long-time D also experiences sustained oscillation. However the maximum value D_{max} is still given by (7.6). These observations are indeed well borne out by the numerical results (SS1, figure 19).

8. Results

The preceding analysis has obtained three different expressions (4.27), (5.21), and (6.8) for the deformation D (7.6) in a time-periodic extensional flow. We first compare these analytical results with those obtained by numerical computations in SS1. This serves two purposes: the accuracy of the numerical solution is verified, and the limitations and applicability of the first-order perturbation results are established. Then we perform a detailed study of the analytical results, varying relevant parameters. The Bessel functions of the complex arguments were computed by recurrence relations and series expansions (Abramowitz & Stegun 1972, p. 358). A clarification of our terminology is in order, as we plot results from a number of different approximations to the same physical problem. We use 'unsteady Stokes' for results from the first-order small-deformation analysis of unsteady governing equations, namely Navier–Stokes without the advective terms. By 'Stokes' we refer to the results from a similar small-deformation first-order analysis of the Stokes equations. Note that the latter encompasses both steady and unsteady imposed flow fields, and the deformation process itself is always time-dependent when transient effects are included. The numerical finite Reynolds number results from SS1 will be referred to as 'numerical'. Finally, in figure 1, we include results from boundary element simulation of arbitrarily large deformation governed by the Stokes equation, provided by Michael Loewenberg and Martin Nemar of Yale University. We refer to their results as the 'BEM solution'.

8.1. *Comparison with numerical solutions of SS1*

In SS1, we computed two-dimensional drop shape at non-zero Reynolds number for a class of time-periodic extensional flows. The rotational extensional flow with $\boldsymbol{u}^{\infty} = \boldsymbol{u}^{RE}$ (7.1) has been studied most extensively for three different Reynolds numbers, $Re = 0.1, 1.0$ and 10.0. In this flow the drop was found to achieve an elliptic shape in the long-time limit. The drop shape rotates (note that the drop does not undergo rigid body rotation, but its deformation maintains the same shape) in response to the forcing field, maintaining the same deformation D. As noted in the last section, the first-order analytical theory is consistent with this observation. The potential vortex is a special case of the rotating extensional (RE) flow, for which frequency $St = 2.0$. For all the values of Re under study, we encounter a resonance phenomenon with increasing interfacial tension or forcing frequency. The long-time D passes through

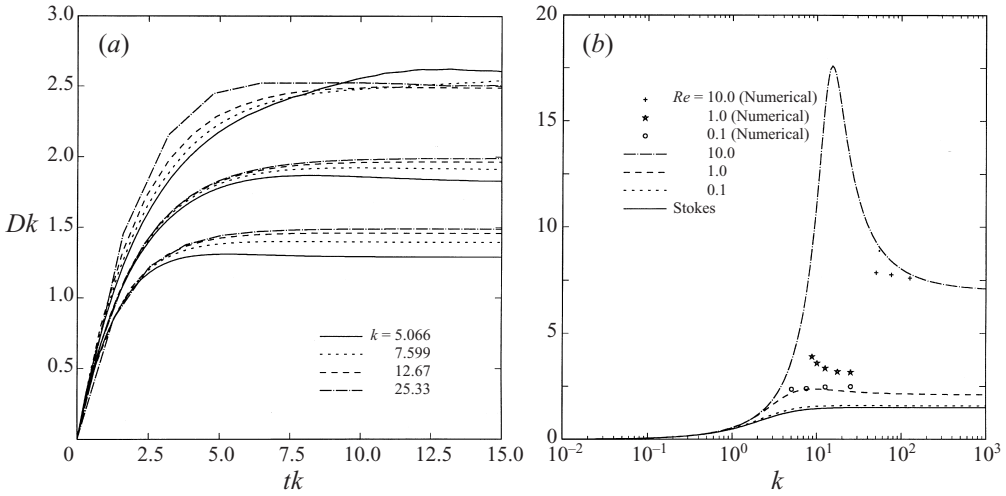

FIGURE 1. Drop response for different interfacial tension in a vortex ($St = 2$) for $Re = 0.1$, $\lambda = \lambda_\rho = 1.0$. (*a*) Evolution with time: top curves, numerical results in SS1; middle curves, BEM solution of the Stokes equation provided by Michael Loewenberg and Martin Nemer; bottom curves, first-order Stokes flow analysis. (*b*) Long-time drop response with varying interfacial tension.

a maximum value. We also performed computations for an oscillating extensional flow $\boldsymbol{u}^\infty = \boldsymbol{u}^{OE}$ (7.7). As one would expect, the drop shape in this case undergoes oscillations, extending and contracting along two axes of the imposed flow. The maximum value of D, D_{max} shows the same resonance phenomenon. All the results in this section are for $\lambda = \lambda_\rho = 1.0$, as in SS1.

We briefly first consider the vortex case ($St = 2.0$) in figure 1. For a vortex flow we found in SS1 that smaller values of interfacial tension lead to unbounded stretching of the drop, resulting in breakup. However, large enough interfacial tension leads to an equilibrium shape with progressively lower deformation. Following Cox (1969) we plot numerically computed Dk with kt for $Re = 0.1$ from SS1 in figure 1(*a*), which shows an approximate collapse of different D curves onto each other (the top set of curves). For comparison, Dk from the first-order Stokes analysis (5.22) with periodic forcing ($\beta = 2\mathrm{i}$) is plotted (bottom set of curves) in the same figure (note that the unsteady Stokes analysis is performed only for time-independent long-time periodic response, and therefore is not applicable for this time plot). We observe that the first-order Stokes analysis underpredicts the deformation at this low St even for $Re = 0.1$. Moreover, in contrast to the numerical solution, $D \sim k^{-1}$ for large k has not yet been achieved by the analytical solution for the values of k examined. The difference from the first-order result, which is valid for high k ($\epsilon = k^{-1}$), even for $k = 25.33$, is somewhat puzzling and leads to concern over the accuracy of the numerical solution. However, in SS1 we have successfully performed a convergence study, and provided a satisfactory match with the analytic results of Buckmaster & Flaherty (1973) for steady extensional flow. On the other hand, the long-time first-order Stokes result (5.22) for a steady extensional flow (i.e. $t \to \infty$ and $\beta = 0$) displays a linear variation with k^{-1}, and similarly underpredicts the deformation obtained by Buckmaster & Flaherty (1973). Furthermore, the actual shapes (not plotted here) from the first-order Stokes and the numerical solutions match reasonably well for high k values, e.g. $k = 25.33$. Also, note that the observed collapse of the curves plotted in the (Dk, tk) plane has surprisingly, in essence, eliminated the significance of the difference in k

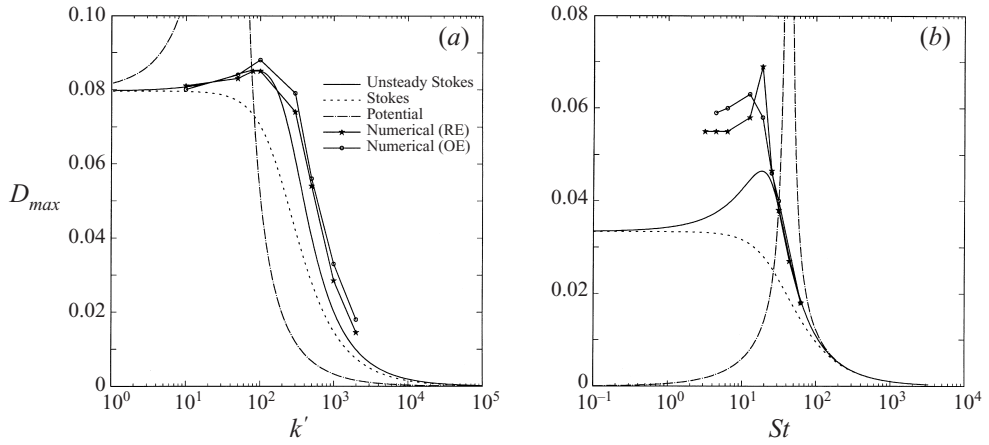

FIGURE 2. Long-time drop response for $Re = 0.1$, $\lambda = \lambda_\rho = 1.0$, ($a$) with varying interfacial tension at $St = 4\pi$, and (b) with varying frequency at $k' = 10k = 450$.

values. In other words, the very fact that different k-curves collapse indicates that the first-order result for a larger k value is no more valid than that for a smaller one.

To investigate the issue further, we also plotted in the same figure Stokes flow boundary integral results (middle set of curves). They too deviate from the first-order Stokes, but approach the finite Reynolds number solution, and in fact lie between the two as expected; the BEM solution predicts a larger deformation compared to the first-order small-deformation analysis, and finite inertia leads to an even larger deformation. In light of these observations, we conclude that our numerical simulation is adequately accurate (see the discussion on convergence in SS1), and the anomaly is in the nature of the quantity, D, in that its next-order corrections in ϵ or Re are not necessarily small. We will make more comments on the difference between numerical and perturbative results in the following.

In figure 1(b) the long-time deformation (from unsteady Stokes analysis) as a function of k has been plotted for different Re. (Note that the analytical result is a function of $\alpha = (1 - \mathrm{i})\sqrt{St\,Re/2}$.) It shows that the analysis predicts the correct trend of the numerical result for large k. For $Re = 0.1$, the unsteady term in the perturbation does not make up for the difference between the numerical and the first-order Stokes result mentioned before. However, note that the perturbation (unsteady Stokes) compares better with the numerical solution for larger Reynolds number, $Re = 10.0$. We believe this to be fortuitous. Drop deformation in a vortex does not show resonance because of the low frequency value $St = 2.0$. In an RE flow both interfacial tension and rotation (frequency) inhibit stretching. In the case of a vortex, for low interfacial tension, the frequency is not sufficiently large to retard the growth. Therefore the ascending portion of the D, k curve is not realized. In fact from (5.21) we obtain $D = 0.5$ for $k = 0$. Therefore the small-deformation assumption allowing the perturbation analysis is violated, and indeed in the numerical simulation we obtain unbounded growth. In the following we concentrate on the resonance behaviour shown by RE and OE flows.

In figure 2(a), we plot the curves for D (or D_{max} for OE flow) from numerical simulations and their analytical counterparts for $Re = 0.1$, as a function of interfacial tension k', for a fixed forcing frequency, $St = \omega/\dot{\gamma} = 4\pi$. The non-dimensional variable $k = Ca^{-1} = \sigma/(\dot{\gamma}\mu a)$, appearing in unsteady Stokes and ordinary Stokes

flow, is not defined in potential flow. Therefore in the following we have used $k' = \sigma/(\rho\dot{\gamma}^2 a^3) = k/Re$, wherever we have compared with potential flow results. As can be seen clearly, the resonance is quantitatively matched. In contrast the simple Stokes solution compares well everywhere but in the region of resonance. The inviscid solution marked by the dash-and-dotted line displays an unbounded response near resonance, as is characteristic of an undamped system. The numerical simulation with finite Reynolds number, even at as small a value as $Re = 0.1$, displays inertial effects. Such a system under periodic forcing behaves as a forced damped oscillator, the viscosity playing the role of a damper, interfacial tension that of a spring, and the flow being the forcing factor. Such an oscillator displays resonance when the forcing frequency matches the natural frequency determined by the mass and the spring constant. In the Stokes limit, owing to the absence of inertia the 'mass' part of the oscillator disappears, taking with it the resonance. In fact (5.20) for the Stokes solution when compared with (6.7) for the inviscid flow, shows the different nature of the equations. The latter is a second-order differential equation, whereas the former is a first-order equation. The peak position of the 'true resonance' as depicted in the inviscid solution at $k' = 4\pi^2$ is different from the unsteady Stokes solution. However such a shift is consistent with the response of a damped and undamped simple harmonic oscillator. For small k', all curves reach a limit $0.08 \sim (4\pi)^{-1} = St^{-1}$, as the drop surface is being passively advected by the flow. This can be verified from (5.21) and (6.8), for the present case of $\lambda = \lambda_\rho = 1$. However it should be noted that the potential and Stokes results would lead to different limits for general values of λ and λ_ρ. Note also that for high k', even though the trends are similar to the numerical solution, owing to their leftward shift the perturbation underpredicts deformation for any particular value of k'.

In figure 2(*b*), we plot the deformation as a function of forcing frequency St, for $k' = 450$ ($k = 45$ for the unsteady and the steady Stokes solutions). The other parameters are kept at the same values as before. Here too we see the resonance structure with the forcing frequency. In this case the forcing frequency is varied and the natural frequency is kept constant. As was mentioned for the vortex case in figure 1, the analytic curve substantially underpredicts the level of the deformation for lower values of St. The Stokes curve again matches the unsteady Stokes outside the resonance region. The inviscid curve with peak at $St = \sqrt{4k'} = 42.43$, shifts to the right in contrast with the previous case for interfacial tension variation. In the zero frequency limit potential flow deformation (6.8) vanishes, for the forcing here is proportional to the frequency.

Next we consider the numerical simulation performed at an intermediate Reynolds number of $Re = 1.0$. In figure 3(*a*), we plot D as a function of k' at a fixed value of forcing frequency $St = 4\pi$, the other parameters kept at the same values as before. Note that the resonance occurs at the same value $k' = 4\pi^2$ as before. Here the resonance is much more prominent compared to that in figure 2(*a*), because of the higher value of Re, which heightens the effects of inertia. Both the RE and OE forcing flows are close to each other, and they compare satisfactorily with the unsteady Stokes solution. Note that the inviscid solution is unchanged from that in figure 2(*a*). The pure Stokes solution is different from that in figure 2(*a*), because k scales differently with k' due to increased Re – here $k = k'$, but in figure 2(*a*) $k = 0.1k'$. In figure 3(*b*), we plot D for varying forcing frequency St at $k = k' = 200$, the other parameters being the same as before. The resonance predicted by the potential solution occurs at $St = 28.28$. Again, resonance is more prominent than that of figure 2(*b*) at lower Re. Note that the potential flow solution is different from that in figure 2(*b*), as k'

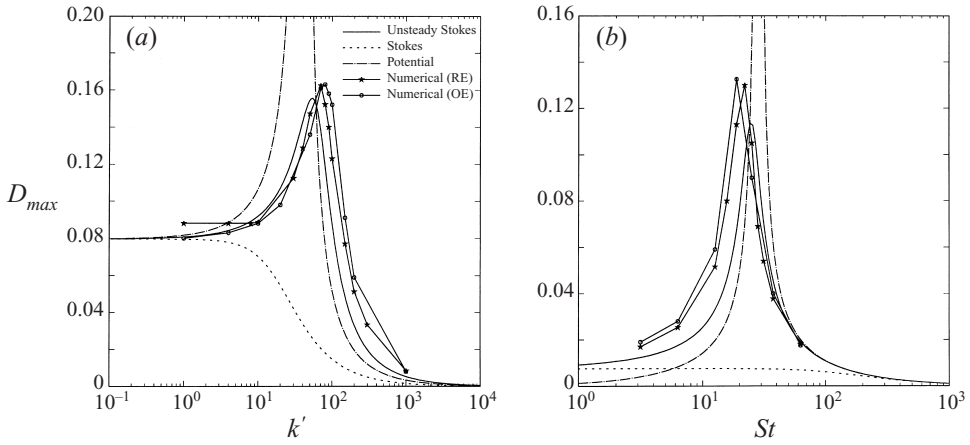

FIGURE 3. Long-time drop response for $Re = 1.0$, $\lambda = \lambda_\rho = 1.0$, ($a$) with varying interfacial tension at $St = 4\pi$, and (b) with varying frequency at $k' = k = 200$.

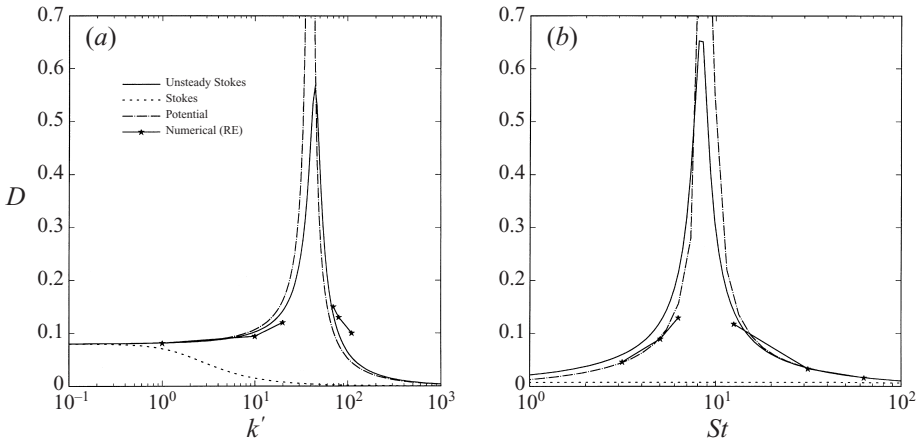

FIGURE 4. Long-time drop response for $Re = 10.0$, $\lambda = \lambda_\rho = 1.0$, ($a$) with varying interfacial tension at $St = 4\pi$, and (b) with varying frequency at $k' = 0.1k = 20$.

is different. Note the underprediction by perturbative methods at high k' (figure 3a) and low St (figure 3b) similar to the lower Reynolds number case.

In SS1, it proved difficult to obtain reliable long-time results over the desired parameter range (especially near resonance) at $Re = 10.0$. In figure 4 those results are compared to the corresponding analytical solutions. One notes from figure 4(a) that at sufficiently low k' the long-time D compares well with all the analytical results. However near resonance ($30 < k' < 60$), even the unsteady Stokes solution predicts $D \simeq 0.6$. Hence the basic assumption of small deformation, on which the perturbation analysis rests, is invalid. This is also the range in which a single long-time numerical value was not available. figure 4(b) shows similar behaviour for varying frequency at a fixed k'. In a small range of frequencies around resonance (at $St = 8.94$) the unsteady Stokes solution predicts too high a value of deformation, where the numerical solution also does not settle down to a long-time steady value.

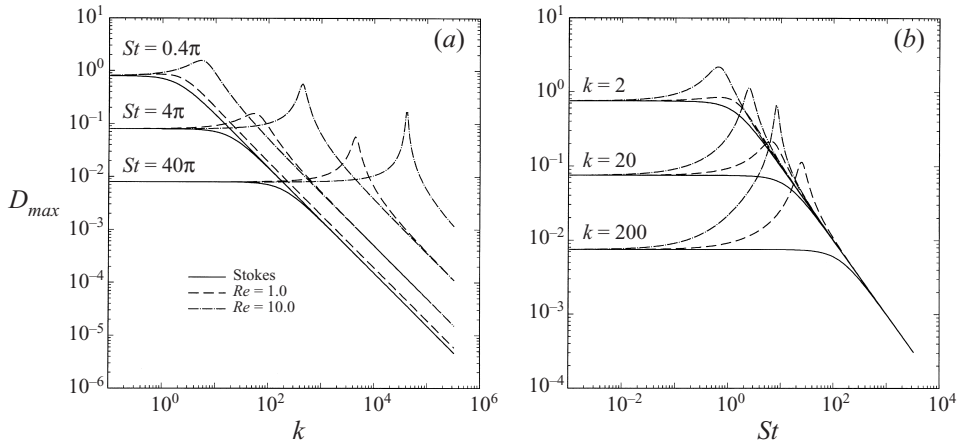

FIGURE 5. Long-time drop response for $\lambda = \lambda_\rho = 1.0$, (*a*) with varying interfacial tension for different *Re* and frequency, and (*b*) with varying frequency for different *Re* and interfacial tension.

8.2. *Parametric study*

We have established that the first-order unsteady Stokes result is sufficient for predicting deformation as long as the deformation is small (e.g. $D < 0.3$). We now turn to study the effects of varying different non-dimensional parameters on these expressions.

In figure 5(*a*) effects of forcing frequency and Reynolds number on deformation are examined as a function of interfacial tension. As has already been seen, for other parameter values fixed, increasing *Re* leads to resonance at higher k. Increased inertia requires larger surface tension to retain the same natural frequency. Increasing frequency inhibits growth. If the frequency is lowered sufficiently (approaching steady extension), one would not expect an equilibrium drop shape at the limit of zero interfacial tension, as is indeed the case for steady extension (Stone 1994). For instance at $St = 0.4\pi$, the limiting value of the deformation at low k is a very large value, $D = 0.8$, which indicates failure of the perturbation theory. In fact in this case, one can show that the full solution would result in an unbounded extension. For such a low frequency case a high interfacial tension is required to obtain a bounded shape (the decreasing portion of the curve). Therefore for such a case, e.g. in a potential vortex, we do not see any resonance. With increasing forcing frequency resonance occurs at a higher value of k, because higher k and thereby higher interfacial tension leads to higher natural frequency. Close scrutiny reveals interesting patterns in these curves. The plot for $St = 0.4\pi$, $Re = 10.0$ converges to that for $St = 4\pi$, $Re = 1.0$, and similarly those for $St = 4\pi$, $Re = 1.0$ with $St = 40\pi$, $Re = 1.0$. This observation indicates that for larger k the governing parameter is $St\,Re$. In fact note that the unsteady term in the governing equation is of the order $\alpha^2 = -\mathrm{i}St\,Re$. Indeed, the Appendix of SS1 predicts that for large k, the k^{-1} decay observed here depends only on $Re\ St$. For different values of St, the Stokes solutions (the solid lines) finally converge for large enough interfacial tension in a single k^{-1} decay as has indeed been predicted by the Appendix of SS1. Also the $k \to 0$ limit is the same for all *Re*. For $\lambda = \lambda_\rho = 1$ the drop is passively advected with the forcing flow, and therefore the shape depends only on St.

Figure 5(*b*) shows the same phenomena for St variation. We see that increased interfacial tension and decreased Reynolds number predictably lead to higher natural

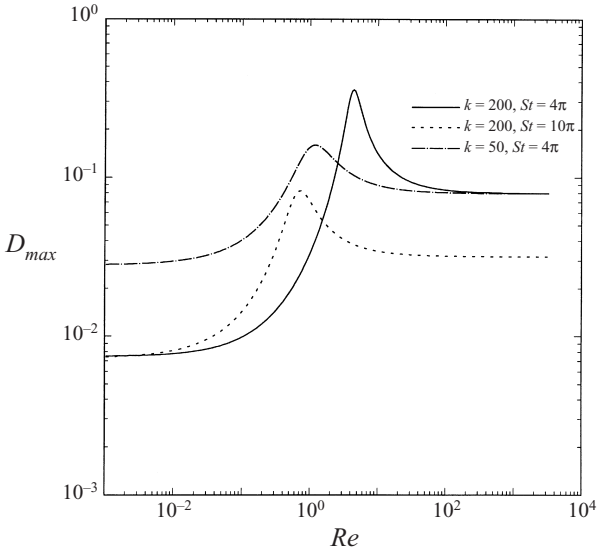

FIGURE 6. Long-time drop response with varying Re; $\lambda = \lambda_\rho = 1.0$.

frequency. The curve for $k = 2$ approaches $D = 0.8$, indicating a failure of the perturbation method. Numerical solution shows that at this low value of interfacial tension and at the limit of zero frequency there is no equilibrium shape, as has been mentioned before. In contrast to figure 5(a), all the curves converge at high frequency, as $D_{max} \rightarrow St^{-1}$ independent of Re and k (shown in Appendix of SS1). The zero frequency limit is a function only of k (again shown in the Appendix of SS1), and hence is independent of Re.

In figure 6, we plot D as a function of Re for $k = 200$ and $St = 4\pi$ (solid line). It too shows characteristic resonance – changing Re is like changing the 'mass' component, and that changes the natural frequency. The effect of changing frequency is displayed by plotting the same for $St = 10\pi$, the other parameters remaining the same. It has a maximum at a lower Re, i.e. with lower forcing frequency the resonance occurs at a lower inertia. The Stokes limit ($Re \rightarrow 0$) is the same in spite of different St because of the large value of k (see the large-k limit of figure 5(a) and the discussion in the text). At a lower value of k, namely, $k = 50$ indicated by the dash-and-dotted curve, resonance occurs again at lower Re than the solid curve, because reduced interfacial tension at the same forcing frequency is matched with less inertia. It should be noted that the high Reynolds number limit of these curves is not the same as that of an inviscid potential flow, as there $k = \sigma/(\dot{\gamma}\mu a) \rightarrow \infty$ and leads to a finite $k' = k/Re$. The high-Re limit here is St^{-1}, as has been predicted in the Appendix of SS1.

In figure 7, we investigate the effects of λ different from unity, for $Re = 1.0$. D plotted as a function of k, at $St = 4\pi$, shows that with increasing λ the resonance peak decreases; an increase in drop viscosity leads to enhanced damping. The curves for $\lambda = 0.01$ and $\lambda = 0.1$ indicate insensitivity to λ for $\lambda < 0.1$. The $k \rightarrow 0$ limit for $\lambda = 1.0$ is the case of a drop passively advected by the flow. As noted before, the high-k limit is independent of all parameters except $St\,Re$. At a fixed $k(= 200)$ also, with increasing λ the peak becomes less prominent. The low- and high-St limits are independent of λ as indeed was predicted in the Appendix of SS1. One notes that variation in λ, as it is only a damping factor, merely changes the strength of the peak, but does not shift its position significantly.

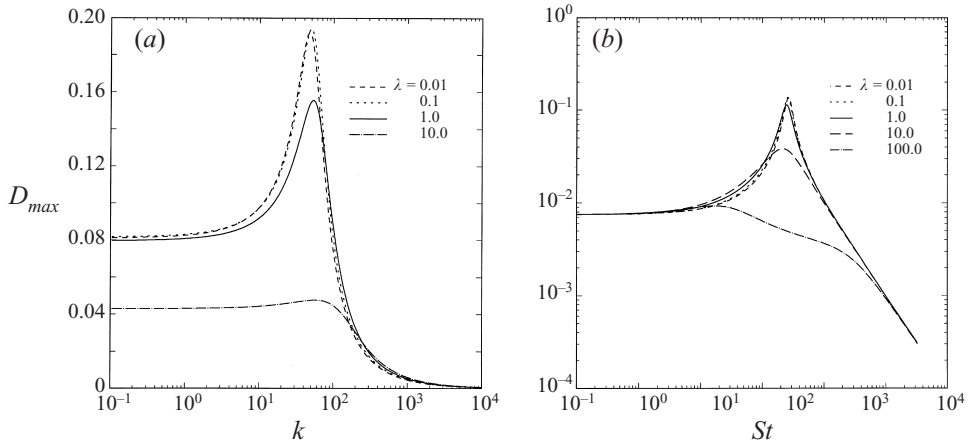

FIGURE 7. Long-time drop response for $Re = 1.0$, $\lambda_\rho = 1.0$, (*a*) with varying interfacial tension at $St = 4\pi$, for different λ, and (*b*) with varying frequency at $k = 200$ for different λ.

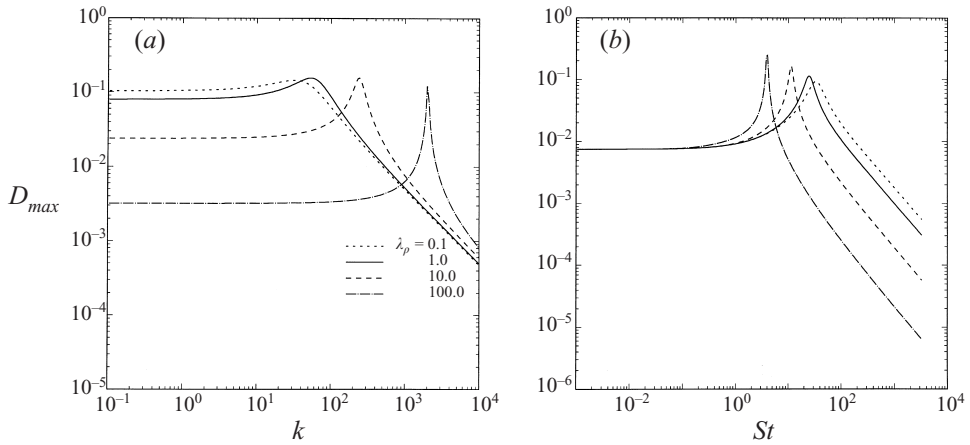

FIGURE 8. Long-time drop response for $Re = 1.0$, $\lambda = 1.0$, (*a*) with varying interfacial tension at $St = 4\pi$ for different λ_ρ, and (*b*) with varying frequency at $k = 200$ for different λ_ρ.

The effects of λ_ρ have been investigated by plotting D as a function of k for four values of λ_ρ in figure 8. Increasing λ_ρ increases the inertia of the system as evident clearly from the inviscid equation (6.7). Therefore for same value of forcing frequency with lower λ_ρ, resonance would occur at lower values of interfacial tension. On the other hand for fixed tension increased λ_ρ leads to decreased natural frequency. These figures are similar in character to those for Re variations, for both Re and λ_ρ change the inertia of the system. As shown in the Appendix of SS1, the high-k limit for a fixed St is independent of λ_ρ, but the high St limit for a fixed k does depend on λ_ρ. In fact it follows $(1 + \lambda_\rho)^{-1}$, as predicted in the Appendix of SS1.

Finally in figure 9, we have plotted D as a function of λ (solid) and λ_ρ (dotted) for $Re = 1.0$, $St = 4\pi$, and $k = 200$. With λ_ρ there is a more prominent resonance as it directly relates to the inertia of the system.

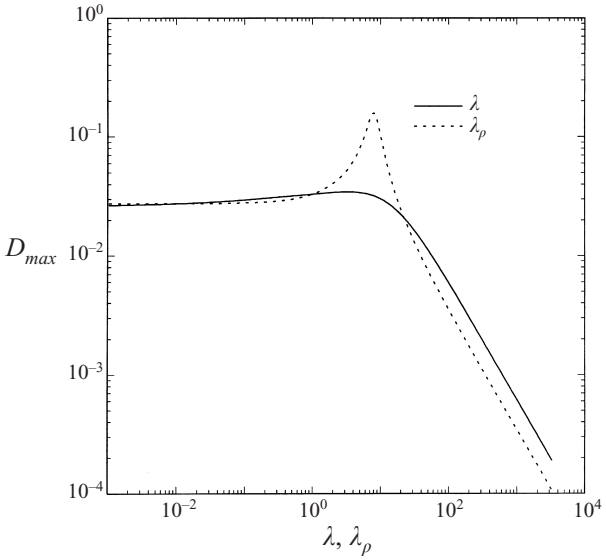

FIGURE 9. Drop response with varying λ_ρ and λ; $Re = 1.0$, $St = 4\pi$, $k = 200$.

9. Summary

A first-order perturbation method is applied to an unsteady Stokes analysis of a two-dimensional drop in time-periodic extensional flows. The results show important features of the time-periodic deformation amplitude. In particular, the analytical solution quantitatively captures a resonance phenomenon previously found in numerical calculations (SS1). The resonance is a direct consequence of the presence of inertia in the unsteady drop behaviour and is not predicted from a pure Stokes solution. Comparison with numerical results also shows the limitations of the first-order perturbation scheme. We note that the perturbation method underpredicts deformation for low frequencies (such as in a vortex) as well as for high interfacial tension. Particularly, the large discrepancy in the vortex case between the numerical result at finite but low Reynolds number, $Re = 0.1$, and solutions obtained by perturbation and BEM have been carefully investigated. One concludes that the deformation criterion D might be too sensitive to be an appropriate measure of the overall drop shape. This is important to recognize when modelling the effects of deformation on rheology of an emulsion.

Retention of the unsteady term and not the convective term in the momentum equation is of course determined by ordering of the former by $St\,Re$, and the latter by Re. The analysis is therefore valid for vanishing Re, yet large St. However, even for $Re \sim O(1)$, for large enough St, the deformation is small (making the first-order theory accurate), and the response is dominated by the acceleration due to the unsteady term. Therefore neglecting the convective term is still justified.

Because the analytical procedure is far less expensive than the numerical solution, we were able to explore a range of parameter space including St, Re, k, λ and λ_ρ. At zero Reynolds number, only k, St and λ appear in the analysis. Here all the parameters are shown to have significant effects, particularly on resonance. Re and λ_ρ are inertial effects, k, representing interfacial tension, provides the spring constant, and together they determine the natural frequency of the system. Resonance occurs when the natural frequency matches with the forcing frequency St. The damping of

the resonance is controlled by λ. The deformation is seen to display a number of interesting scaling behaviours with different parameters that are explained by the simple ODE model described in the Appendix of SS1.

The authors gratefully acknowledge the codes received from Dr Hasan Oguz of The Johns Hopkins University for computation of the Bessel functions for complex arguments. The data for the numerical Stokes flow solution by BEM in figure 1 were graciously provided by Professor Michael Loewenberg and Martin Nemer of Yale University. Comments of Professors Howard Stone, Michael Loewenberg, and the reviewers have helped us to improve the presentation.

Appendix A

In this appendix, we provide the velocity and the stress expressions appearing in (4.11)–(4.15) for the unsteady Stokes flow. They are evaluated at the surface $r = 1$. Henceforth use $J_n = J_n(\alpha^*)$ and $H_n = H_n^{(2)}(\alpha)$.

$$u_r = u_r^\infty + \left(\frac{\partial\phi}{\partial r} + \frac{1}{r}\frac{\partial\psi}{\partial\theta}\right)_{r=1} = \sum_n \left(E_{11}\delta_{n2} - \frac{n}{\alpha^2}T_n + nH_n\tilde{U}_n\right)\cos n\theta + \sum_n \left(E_{12}\delta_{n2} - \frac{n}{\alpha^2}\tilde{T}_n - nH_nU_n\right)\sin n\theta, \quad \text{(A 1)}$$

$$u_r^* = \left(\frac{\partial\phi^*}{\partial r} + \frac{1}{r}\frac{\partial\psi^*}{\partial\theta}\right)_{r=1} = \sum_n \left(\frac{n}{\alpha^{*2}}T_n^* + nJ_n\tilde{U}_n^*\right)\cos n\theta + \sum_n \left(\frac{n}{\alpha^{*2}}\tilde{T}_n^* - nJ_nU_n^*\right)\sin n\theta, \quad \text{(A 2)}$$

$$u_\theta = \left(u_\theta^\infty + \frac{1}{r}\frac{\partial\phi}{\partial\theta} - \frac{\partial\psi}{\partial r}\right)_{r=1} = \sum_n \left(E_{12}\delta_{n2} + \frac{n}{\alpha^2}\tilde{T}_n - \alpha H_n'U_n\right)\cos n\theta + \sum_n \left(-E_{11}\delta_{n2} - \frac{n}{\alpha^2}T_n - \alpha H_n'\tilde{U}_n\right)\sin n\theta, \quad \text{(A 3)}$$

$$u_\theta^* = \left(\frac{1}{r}\frac{\partial\phi^*}{\partial\theta} - \frac{\partial\psi^*}{\partial r}\right)_{r=1} = \sum_n \left(\frac{n}{\alpha^{*2}}\tilde{T}_n^* - \alpha^*J_n'U_n^*\right)\cos n\theta + \sum_n \left(-\frac{n}{\alpha^{*2}}T_n^* - \alpha^*J_n'\tilde{U}_n^*\right)\sin n\theta, \quad \text{(A 4)}$$

$$\begin{aligned} p_{rr} &= \left[-(p^\infty + p) + 2e_{rr}^\infty + 2\left(\frac{\partial^2\phi}{\partial r^2} - \frac{1}{r^2}\frac{\partial\psi}{\partial\theta} + \frac{1}{r}\frac{\partial^2\psi}{\partial r\partial\theta}\right)\right]_{r=1} \\ &= \sum_n \left\{-\left(\frac{\alpha^2}{2} - 2\right)E_{11}\delta_{n2} - \left(1 - \frac{2n(n+1)}{\alpha^2}\right)T_n - 2n(H_n - \alpha H_n')\tilde{U}_n\right\}\cos n\theta \\ &\quad + \sum_n \left\{-\left(\frac{\alpha^2}{2} - 2\right)E_{12}\delta_{n2} - \left(1 - \frac{2n(n+1)}{\alpha^2}\right)\tilde{T}_n + 2n(H_n - \alpha H_n')U_n\right\}\sin n\theta, \end{aligned} \quad \text{(A 5)}$$

$$p^*_{rr} = \left[-p^* + 2\left(\frac{\partial^2\phi^*}{\partial r^2} - \frac{1}{r^2}\frac{\partial\psi^*}{\partial\theta} + \frac{1}{r}\frac{\partial^2\psi^*}{\partial r\partial\theta}\right)\right]_{r=1}$$
$$= \sum_n \left\{-\left(1 - \frac{2n(n-1)}{\alpha^{*2}}\right) T^*_n - 2n(J_n - \alpha^* J'_n)\tilde{U}^*_n\right\}\cos n\theta$$
$$+ \sum_n \left\{-\left(1 - \frac{2n(n-1)}{\alpha^{*2}}\right) \tilde{T}^*_n + 2n(J_n - \alpha^* J'_n)U^*_n\right\}\sin n\theta, \qquad \text{(A 6)}$$

$$p_{r\theta} = \left[2e^\infty_{r\theta} + 2\left(\frac{1}{r}\frac{\partial^2\phi}{\partial r\partial\theta} - \frac{1}{r^2}\frac{\partial\phi}{\partial\theta} - \frac{\partial^2\psi}{\partial r^2} - \frac{\alpha^2}{2}\psi\right)\right]_{r=1}$$
$$= \sum_n 2\left\{E_{12}\delta_{n2} - \frac{n^2+n}{\alpha^2}\tilde{T}_n - \alpha^2(H''_n + \tfrac{1}{2}H_n)U_n\right\}\cos n\theta$$
$$+ \sum_n 2\left\{-E_{11}\delta_{n2} + \frac{n^2+n}{\alpha^2}T_n - \alpha^2(H''_n + \tfrac{1}{2}H_n)\tilde{U}_n\right\}\sin n\theta, \qquad \text{(A 7)}$$

$$p^*_{r\theta} = \left[2\left(\frac{1}{r}\frac{\partial^2\phi^*}{\partial r\partial\theta} - \frac{1}{r^2}\frac{\partial\phi^*}{\partial\theta} - \frac{\partial^2\psi^*}{\partial r^2} - \frac{\alpha^{*2}}{2}\psi^*\right)\right]_{r=1}$$
$$= \sum_n 2\left\{\frac{n^2-n}{\alpha^{*2}}\tilde{T}^*_n - \alpha^{*2}(J''_n + \tfrac{1}{2}J_n)U^*_n\right\}\cos n\theta$$
$$+ \sum_n 2\left\{-\frac{n^2-n}{\alpha^{*2}}T^*_n - \alpha^{*2}(J''_n + \tfrac{1}{2}J_n)\tilde{U}^*_n\right\}\sin n\theta. \qquad \text{(A 8)}$$

Appendix B

Using (4.17)–(4.20), we obtain for (4.21)–(4.24)

$$\left.\begin{aligned} a_{11}U_2 + a_{12}U^*_2 &= 2(E_{12} - \epsilon\beta\tilde{f}_2), \qquad a_{11}\tilde{U}_2 + a_{12}\tilde{U}^*_2 = -2(E_{11} - \epsilon\beta f_2),\\ a_{11} &= (2H_2 + \alpha H'_2), \qquad a_{12} = (2J_2 - \alpha^* J'_2), \end{aligned}\right\} \qquad \text{(B 1)}$$

$$\left.\begin{aligned} a_{21}U_2 + a_{22}U^*_2 &= 2E_{12} - (3-\lambda)\epsilon\beta\tilde{f}_2, \qquad a_{21}\tilde{U}_2 + a_{22}\tilde{U}^*_2 = -\{2E_{11} - (3-\lambda)\epsilon\beta f_2\},\\ a_{21} &= \left\{6H_2 - \alpha^2\left(H''_2 + \tfrac{1}{2}H_2\right)\right\}, \qquad a_{22} = -\lambda\left\{2J_2 - \alpha^{*2}\left(J''_2 + \tfrac{1}{2}J_2\right)\right\}. \end{aligned}\right\} \qquad \text{(B 2)}$$

We may solve the set of equations (B 1) and (B 2) to arrive at following solution:

$$\left.\begin{aligned} U_2 &= B_1E_{12} + B_2\epsilon\beta\tilde{f}_2, \qquad U^*_2 = B_3E_{12} + B_4\epsilon\beta\tilde{f}_2\\ B_1 &= 2D_a^{-1}(a_{22} - a_{12}), \qquad B_2 = D_a^{-1}((3-\lambda)a_{12} - 2a_{22}),\\ B_3 &= 2D_a^{-1}(a_{11} - a_{21}), \qquad B_4 = D_a^{-1}(2a_{21} - (3-\lambda)a_{11}), \end{aligned}\right\} \qquad \text{(B 3)}$$

where D_a is the determinant of the 2×2 matrix formed by the component $a_{ij}, i, j = 1, 2$. For the $\sin 2\theta$ components

$$\tilde{U}_2 = -(B_1E_{11} + B_2\epsilon\beta f_2), \qquad \tilde{U}^*_2 = -(B_3E_{11} + B_4\epsilon\beta f_2). \qquad \text{(B 4)}$$

We then find from (4.17)–(4.20) by substitution

$$\left.\begin{aligned} T_2 &= C_1E_{11} + C_2\epsilon\beta f_2, & T_2^* &= C_3E_{11} + C_4\epsilon\beta f_2,\\ C_1 &= -\alpha^2\left(B_1H_2 - \tfrac{1}{2}\right), & C_2 &= -\alpha^2\left(B_2H_2 + \tfrac{1}{2}\right),\\ C_3 &= \alpha^{*2}B_3J_2, & C_4 &= \alpha^{*2}\left(B_4J_2 + \tfrac{1}{2}\right), \end{aligned}\right\} \tag{B 5}$$

and

$$\tilde{T}_2 = C_1E_{12} + C_2\epsilon\beta\tilde{f}_2, \qquad \tilde{T}_2^* = C_3E_{12} + C_4\epsilon\beta\tilde{f}_2. \tag{B 6}$$

Now that we have obtained all the unknown coefficients in terms of the forcing field strain-rate tensor E_{ij}, and the surface function f_2 and $\tilde{f}_2$, we can express the normal stress (4.25) and (4.26) as

$$\left.\begin{aligned} D_1T_2 + D_2T_2^* + D_3\tilde{U}_2 + D_4\tilde{U}_2^* &= \left(\frac{\alpha^2}{2} - 2\right)E_{11} + 4k\epsilon f_2,\\ D_1 = -\left(1 - \frac{12}{\alpha^2}\right),\ D_2 &= \lambda\left(1 - \frac{4}{\alpha^{*2}}\right),\ D_3 = -4(H_2 - \alpha H_2'),\ D_4 = 4\lambda(J_2 - \alpha^*J_2'), \end{aligned}\right\} \tag{B 7}$$

$$D_1\tilde{T}_2 + D_2\tilde{T}_2^* - D_3U_2 - D_4U_2^* = \left(\frac{\alpha^2}{2} - 2\right)E_{12} + 4k\epsilon\tilde{f}_2. \tag{B 8}$$

Upon substituting (B 3)–(B 6), the final equations are

$$\begin{aligned} &\{\beta(D_1C_2 + D_2C_4 - D_3B_2 - D_4B_4) - 4k\}\epsilon f_2\\ &\qquad = \left(\frac{\alpha^2}{2} - 2 - D_1C_1 - D_2C_3 + D_3B_1 + D_4B_3\right)E_{11}, \end{aligned} \tag{B 9}$$

and an identical equation relating the odd components $\tilde{f}_2$ to E_{12}. We can substitute the expressions for f back to obtain the other coefficients, and obtain velocity and pressure in the entire domain.

Appendix C

Here we provide the expressions for velocity and stress for Stokes flow evaluated at $r = 1$:

$$u_r = \left(u_r^\infty + \frac{1}{r}\frac{\partial\psi}{\partial\theta}\right)_{r=1} = (E_{12} - 2U_2 - \tilde{T}_2)\sin 2\theta + (E_{11} + 2\tilde{U}_2 + T_2)\cos 2\theta, \tag{C 1}$$

$$u_r^* = \left(\frac{1}{r}\frac{\partial\psi^*}{\partial\theta}\right)_{r=1} = (-2U_2^* - \tilde{T}_2^*)\sin 2\theta + (2\tilde{U}_2^* + T_2^*)\cos 2\theta, \tag{C 2}$$

$$u_\theta = \left(u_\theta^\infty - \frac{\partial\psi}{\partial r}\right)_{r=1} = (-E_{11} + 2\tilde{U}_2)\sin 2\theta + (E_{12} + 2U_2)\cos 2\theta, \tag{C 3}$$

$$u_\theta^* = \left(-\frac{\partial\psi^*}{\partial r}\right)_{r=1} = (-2\tilde{U}_2^* - 4T_2^*)\sin 2\theta + (-2U_2^* - 4\tilde{T}_2^*)\cos 2\theta, \tag{C 4}$$

$$\begin{aligned} p_{rr} &= \left[-p + 2e_{rr}^\infty + 2\left(-\frac{1}{r^2}\frac{\partial\psi}{\partial\theta} + \frac{1}{r}\frac{\partial^2\psi}{\partial r\partial\theta}\right)\right]_{r=1}\\ &= (2E_{12} + 8\tilde{T}_2 + 12U_2)\sin 2\theta + (2E_{11} - 8T_2 - 12\tilde{U}_2)\cos 2\theta \end{aligned} \tag{C 5}$$

$$p^*_{rr} = \left[-p^* + 2\left(-\frac{1}{r^2}\frac{\partial\psi^*}{\partial\theta} + \frac{1}{r}\frac{\partial^2\psi^*}{\partial r\partial\theta}\right)\right]_{r=1}$$
$$= (12\tilde{T}^*_2 - 4U^*_2)\sin 2\theta + (-12T^*_2 - 4\tilde{U}^*_2)\cos 2\theta \quad \text{(C 6)}$$

$$p_{r\theta} = \left[2e^{\infty}_{r\theta} + 2\left(-\frac{1}{2}\frac{\partial^2\psi}{\partial r^2} + \frac{1}{2r}\frac{\partial\psi}{\partial r} + \frac{1}{2r^2}\frac{\partial^2\psi}{\partial^2\theta}\right)\right]_{r=1}$$
$$= 2(-E_{11} - 6\tilde{U}_2 - 2T_2)\sin 2\theta + 2(E_{12} - 6U_2 - 2\tilde{T}_2)\cos 2\theta, \quad \text{(C 7)}$$

$$p^*_{r\theta} = 2\left[-\frac{1}{2}\frac{\partial^2\psi^*}{\partial r^2} + \frac{1}{2r}\frac{\partial\psi^*}{\partial r} + \frac{1}{2r^2}\frac{\partial^2\psi^*}{\partial^2\theta}\right]_{r=1}$$
$$= 2(-2\tilde{U}^*_2 - 6T^*_2)\sin 2\theta + 2(-2U^*_2 - 2\tilde{T}^*_2)\cos 2\theta. \quad \text{(C 8)}$$

REFERENCES

Abramowitz, M. & Stegun, I. A. 1972 *Handbook of Mathematical Functions.* Dover.

Barthès-Biesel, D. & Acrivos, A. 1973 Deformation and burst of a liquid droplet freely suspended in a linear shear field. *J. Fluid Mech.* **61**, 1–21.

Bentley, B. J. & Leal, L. G. 1986*a* A computer-controlled four-roll mill for investigations of particle and drop dynamics in a two-dimensional linear shear flow. *J. Fluid Mech.* **167**, 219–240.

Bentley, B. J. & Leal, L. G. 1986*b* An experimental investigation of drop deformation and breakup in steady, two-dimensional linear flow. *J. Fluid Mech.* **167**, 241–283.

Buckmaster, J. D. & Flaherty, J. E. 1973 The bursting of two-dimensional drops in slow viscous flow. *J. Fluid Mech.* **60**, 625–639.

Cox, R. G. 1969 The deformation of a drop in a general time-dependent fluid flow. *J. Fluid Mech.* **37**, 601–623.

Frankel, N. A. & Acrivos, A. 1970 The constitutive equation for a dilute emulsion. *J. Fluid Mech.* **44**, 65–78.

Fung, Y. C. 1965 *Foundation of Solid Mechanics.* Prentice-Hall.

Hakimi, F. S. & Schowalter, W. R. 1980 The effects of shear and vorticity on deformation of a drop. *J. Fluid Mech.* **98**, 635–645.

Lamb, H. 1887 On the oscillations of a viscous spheroid. *Proc. Lond. Math. Soc.* (*1*) **xiii**, 51–66.

Lamb, H. 1932 *Hydrodynamics.* Cambridge University Press.

Landau, L. D. & Lifshitz, E. M. 1987 *Fluid Mechanics.* Pergamon.

Richardson, S. 1968 Two-dimensional bubbles in slow viscous flows. *J. Fluid Mech.* **33**, 476–493.

Richardson, S. 1973 Two-dimensional bubbles in slow viscous flows. Part 2. *J. Fluid Mech.* **58**, 115–127.

Rallison, J. M. 1980 Note on the time-dependent deformation of a viscous drop which is almost spherical. *J. Fluid Mech.* **98**, 625–633.

Rallison, J. M. 1984 The deformation of small viscous drops and bubbles in shear flows. *Ann. Rev. Fluid Mech.* **16**, 4-66.

Sarkar K. & Schowalter, W. R. 2001 Deformation of a two-dimensional drop at non-zero Reynolds number in time-periodic extensional flows: numerical simulation. *J. Fluid Mech.* **436**, 177–206.

Seth, K. S. & Pozrikidis, C. 1995 Effects of inertia on the deformation of liquid drops in simple shear flow. *Intl J. Multiphase Flows* **26**, 65–102.

Stone, H. A. 1994 Dynamics of drop deformation and breakup in viscous fluids. *Ann. Rev. Fluid Mech.* **26**, 65–102.

Taylor, G. I. 1932 The viscosity of a liquid containing small drops of another fluid. *Proc. R. Soc. Lond.* A **138** 41–48.